iScience

CellPress

Article

Mitochondrial Populations Exhibit Differential Dynamic Responses to Increased Energy Demand during Exocytosis *In Vivo*

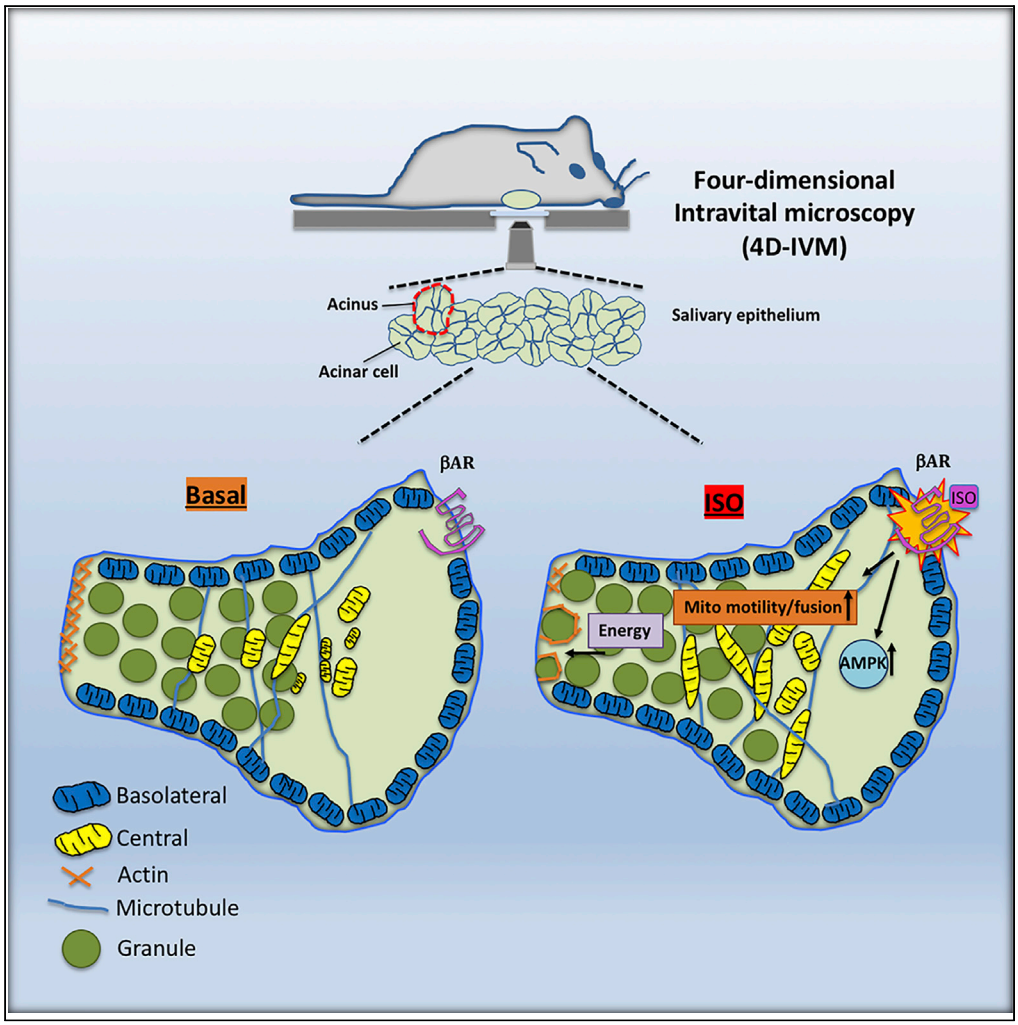

Natalie Porat-Shliom, Olivia J. Harding, Lenka Malec, Kedar Narayan, Roberto Weigert

poratshliomn@mail.nih.gov (N.P.-S.)
weigertr@mail.nih.gov (R.W.)

HIGHLIGHTS

In the salivary glands, mitochondria exist in two populations: basolateral and central

Basolateral mitochondria are static and frequently fuse

Central mitochondria are highly motile and rarely fuse

Exocytosis elicits selective, microtubule-dependent response in central mitochondria

Porat-Shliom et al., iScience *11*, 440–449
January 25, 2019
https://doi.org/10.1016/j.isci.2018.12.036

iScience

CellPress

Article

Mitochondrial Populations Exhibit Differential Dynamic Responses to Increased Energy Demand during Exocytosis *In Vivo*

Natalie Porat-Shliom,[1,2,3,7,*] Olivia J. Harding,[2,6] Lenka Malec,[1] Kedar Narayan,[4,5] and Roberto Weigert[1,2,*]

SUMMARY

Mitochondria are dynamic organelles undergoing fission, fusion, and translocation. These processes have been studied in cultured cells; however, little is known about their regulation in cells within tissues *in vivo*. We applied four-dimensional intravital microscopy to address this in secretory cells of the salivary gland. We found that mitochondria are organized in two populations: one juxtaposed to the basolateral plasma membrane and the other dispersed in the cytosol. Under basal conditions, central mitochondria exhibit microtubule-dependent motility and low fusion rate, whereas basolateral mitochondria are static and display high fusion rate. Increasing cellular energy demand by β-adrenergic stimulation of regulated exocytosis selectively enhanced motility and fusion of central mitochondria. Inhibition of microtubule polymerization led to inhibition of central mitochondrial motility and fusion and a marked reduction in exocytosis. This study reveals a conserved heterogeneity in mitochondrial positioning and dynamics in exocrine tissues that may have fundamental implications in organ pathophysiology.

INTRODUCTION

Mitochondria undergo continuous fission, fusion, and motility, collectively known as mitochondrial dynamics (Hoppins, 2014; Youle and van der Bliek, 2012). These events affect mitochondrial number, morphology, and distribution, thus impacting their bioenergetic capacity (Liesa and Shirihai, 2013; Westermann, 2012). For example, nutrient starvation promotes mitochondrial fusion, giving rise to a network that efficiently produces ATP and protects from mitophagy (Gomes et al., 2011; Rambold et al., 2011). Conversely, mitochondria in neurons, immune cells, and migrating cells undergo fission and transport to sites where ATP is required (Misgeld and Schwarz, 2017; Quintana and Hoth, 2012; Schuler et al., 2017). Thus, different cells have developed distinct mechanisms to rearrange their mitochondrial networks and adapt to changes in energy demand by rearranging their mitochondrial networks. However, the extent to which mitochondrial dynamic rearrangements occur *in vivo* and what physiological cues trigger them are poorly understood. In fact, current views of mitochondrial dynamics in neurons were recently challenged using intravital microscopy in the intact brain of live mice (Faits et al., 2016; Smit-Rigter et al., 2016).

Regulated exocytosis of proteins into saliva is controlled by β-adrenergic signaling, which induces cytoskeleton rearrangement and secretory granules fusion with a narrow canaliculus (Proctor and Carpenter, 2014). We previously speculated that this energetically unfavorable process will require ATP (Masedunskas et al., 2012). Furthermore, we hypothesized that an increase in energy demand during exocytosis will lead to dynamic rearrangement of mitochondria. To this aim, we used four-dimensional intravital microscopy (4D-IVM) in murine salivary glands (SGs). We show that cellular ATP is depleted during exocytosis and that ATP production is necessary to sustain it. Interestingly, we found two populations of mitochondria in salivary acinar cells: basolateral (BL) and central (CEN), with distinct dynamic properties under basal conditions. In response to increased energy demand during β-adrenergic-induced exocytosis, CEN mitochondrial motility and fusion were upregulated in a microtubule (MT)-dependent manner. Finally, inhibiting MT polymerization blocked CEN mitochondrial dynamics and inhibited exocytosis thus suggesting a distinctive role for CEN mitochondrial dynamics in sustaining exocytosis. This study underscores the importance of studying the spatiotemporal regulation of mitochondrial structure and function in intact tissues *in vivo*.

RESULTS

Stimulation of Exocytosis Induces an Acute Change in Energy Demand

The salivary epithelium consists of acinar cells clustered into acini, which respond to β-adrenergic stimulation by exocytosis of secretory granules (see graphical abstract and Masedunskas et al., 2011). To

[1]Laboratory of Cellular and Molecular Biology, National Cancer Institute, National Institutes of Health, Bethesda, MD 20892, USA

[2]National Institute of Dental and Craniofacial Research, National Institutes of Health, Bethesda, MD 20892, USA

[3]Cell Biology and Imaging Section, Thoracic and Gastrointestinal Oncology Branch, National Cancer Institute, National Institutes of Health, Bethesda, MD 20892, USA

[4]Center for Molecular Microscopy, Center for Cancer Research, National Cancer Institute, National Institutes of Health, 8560 Progress Drive, Frederick, MD 21701, USA

[5]Cancer Research Technology Program, Frederick National Laboratory for Cancer Research, Frederick, MD, USA

[6]Present address: Biomedical Graduate Studies Program at the University of Pennsylvania, Philadelphia, PA, USA

[7]Lead Contact

*Correspondence: poratshliomn@mail.nih.gov (N.P.-S.), weigertr@mail.nih.gov (R.W.)

https://doi.org/10.1016/j.isci.2018.12.036

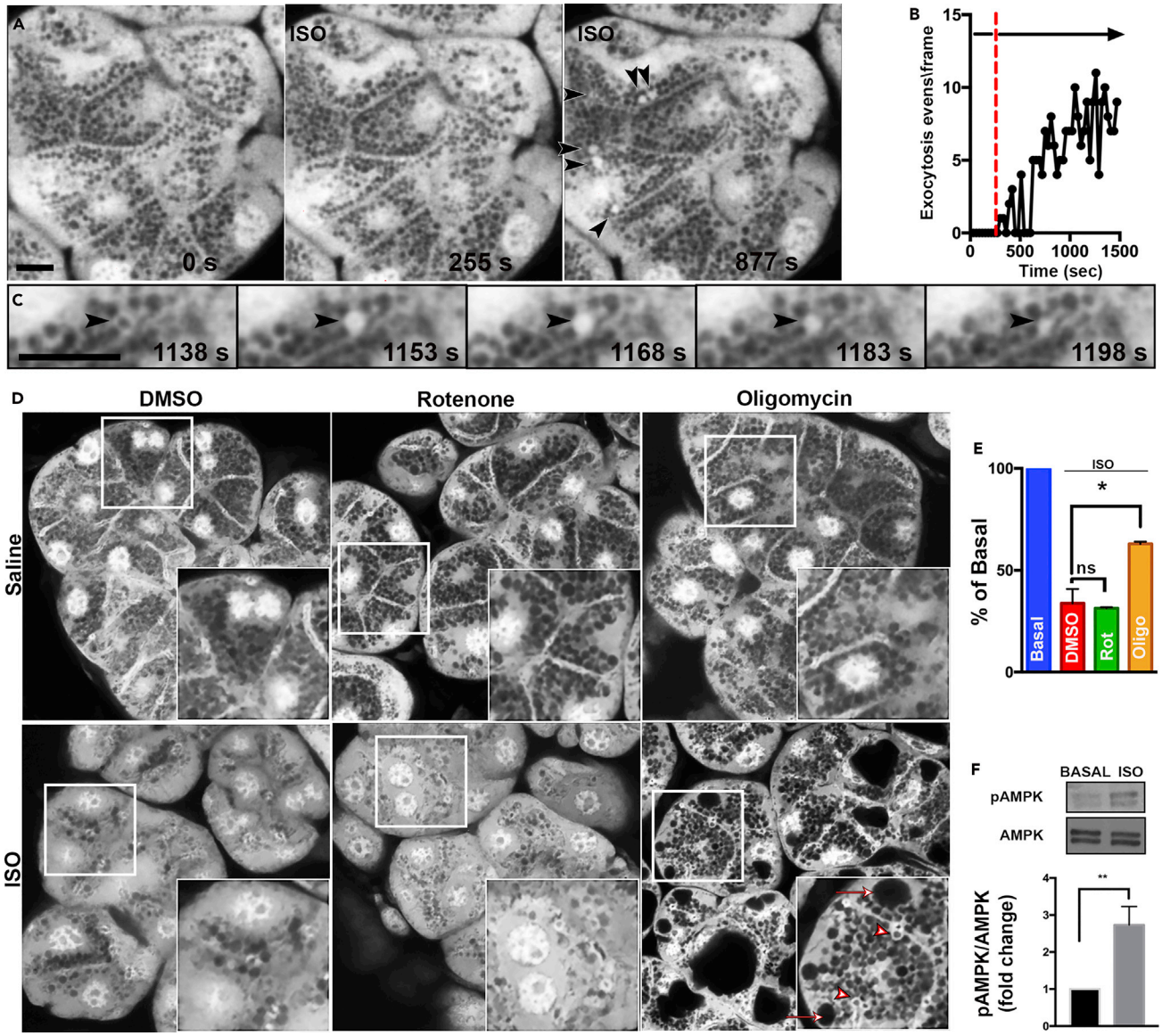

Figure 1. Exocytosis Is an Energy-Dependent Process

(A) 4D-IVM of regulated exocytosis induced by injection of 10 μg/kg ISO in cytosolic-GFP mice. Arrowheads indicate granules undergoing exocytosis.

(B) Number of exocytic events per frame (Video S1).

(C) Single granule undergoing exocytosis.

(D) SGs in cytosolic-GFP mice treated for 20 min with DMSO, 10 μM rotenone, or 1 μg/mL oligomycin followed by saline or ISO injection (30 min). Arrowheads indicate fused granule; arrows indicate large vacuoles.

(E) Exocytosis was evaluated by plotting the normalized number of granules, expressed as percent of the number of granules under basal conditions, 30 min after stimulation under the various treatments.

(F) Fold change in pAMPK/total AMPK 5 min after ISO stimulation.

Results are shown as mean ± SEM in three experiments; *$p < 0.05$, **$p < 0.005$; unpaired t test. Scale bar, 5 μm.

characterize the exocytic response, we applied 4D-IVM in a cytosolic-GFP mouse. About 60 s after β-adrenergic stimulation by subcutaneous isoproterenol (ISO) injection, exocytic events begin in all acinar cells, and the events continue over the course of 25 min (Figures 1A–1C and Video S1). Because exocytosis involves the fusion of large secretory granules into a narrow canaliculus, we previously speculated that this process would require energy in the form of ATP (Masedunskas et al., 2012). To test whether a surge in ATP production sustains exocytosis, complex I and ATP synthase were inhibited using rotenone and oligomycin (Porat-Shliom et al., 2014), respectively, prior to ISO stimulation (Figure 1D). To evaluate exocytosis,

granules were counted, normalized to cell area, and expressed as percent of granule number under basal conditions. ISO stimulation of control cells (DMSO) had only 30% of the granules left (i.e., 70% underwent exocytosis; compare blue bar, basal, with red bar, DMSO; Figure 1E). Oligomycin treatment significantly inhibited exocytosis (Figure 1E) and arrested integration of fused granules into the canaliculi (Figure 1D arrowheads) generating large vacuoles (Figure 1D; arrows). Rotenone had no effect on exocytosis, suggesting that ATP synthase but not complex I is required for this process. Neither drug had an effect on granule number or distribution under basal conditions. Additionally, we found that the AMP:ATP sensor, AMP-Activated Protein Kinase (AMPK), was activated 5 min following exocytosis stimulation, consistent with rapid depletion of cellular ATP (Figure 1F). These results suggest that the onset of exocytosis depletes cellular ATP, leading to AMPK activation and possibly activating the ATP synthase to sustain exocytosis.

Distinct Mitochondrial Subpopulations in SGs

To investigate whether changes in energy demand during exocytosis elicit a change in mitochondrial dynamics, we initially characterized mitochondrial distribution *in vivo* under basal conditions. The SGs of cytosolic-GFP/tandem-Tomato membrane (mTom) mice were labeled with MitoTracker and imaged. Mitochondria were observed both in the cytosol and concentrated along the plasma membrane (PM) (Figure 2A arrowheads, Videos S2 and S3). To determine whether this distribution is random or polarized we compared the number of mitochondria-positive pixels per area for either entire cells or for the area within 2 μm of the PM (see Transparent Methods) and found that the majority (60%) of mitochondria align along the PM (Figures 2B–2D), demarcated by the basolateral marker, NKCC1, but not the apical marker, AQP5 (Figure 2E and Video S4). Other organelles, such as lipid droplets, did not display polarized distribution (Figure S3A). To determine whether these two mitochondrial populations were interconnected, focused ion beam scanning electron microscopy (FIB-SEM) (Narayan et al., 2014) was used to generate 3D datasets of an acinar cell (Figure 2F left). Segmentation, color coding by population (Figure 2F center panel, Video S5), and 3D volume rendering (Figure 2F right panel and Video S6) revealed that both populations comprise discrete mitochondria of various lengths (Figure 2F). Finally, since mitochondrial populations were observed in isolated pancreatic acini (Park et al., 2001), we examined mitochondrial distribution in other exocrine glands, including the pancreas, lacrimal glands, and parotid glands and found the two spatially distinct mitochondrial populations (Figure S1) to be conserved. Hereafter, mitochondrial populations will be referred to as basolateral (BL) and central (CEN) mitochondria, respectively.

Mitochondrial Populations Exhibit Distinct Dynamic Properties under Basal Conditions

Next, we measured mitochondrial motility in the SGs of cytosolic-GFP mice labeled with MitoTracker (see Transparent Methods and Figures S2A–S2G). The BL mitochondria were static, whereas the CEN mitochondria were highly motile with an average displacement of 1.6 μm/min (Figures 3A–3C, and Video S7). Since mitochondrial motility was shown to be dependent on the cytoskeleton (Anesti and Scorrano, 2006), we evaluated the requirement of MTs and/or actin for CEN mitochondrial motility by treating SGs of cytosolic-GFP mice with either 33 μM nocodazole (NZ) or 10 μM cytochalasin D (CD). NZ, but not CD (Figures S2F and S2G), treatment inhibited CEN mitochondrial motility (Figures 3D–3F and Video S8). Consistent with this finding, immunofluorescence showed central mitochondria aligned along MTs (Figures S2H and S2I and Video S9). Interestingly, neither NZ nor CD affected mitochondrial distribution (Figure S2J), suggesting that other tethering mechanisms are involved, possibly through contacts with the ER (Murley and Nunnari, 2016), although we could not confirm this (Figures S2K and S2L).

To determine whether mitochondria undergo fusion *in vivo*, and if so, whether the two populations fuse with each other, we photo converted CEN or BL mitochondria in Mito-Dendra2 mice as described in Transparent Methods (Figures 3G and 3H and Video S10). Interestingly, BL converted signal took 30–40 min to double in volume (Figure 3J), whereas CEN converted signal took over 3 h to do the same (Figure 3I). Fusion between the two populations was rarely observed (Video S10, time: 4:05:53). In summary, under basal conditions, CEN and BL mitochondria demonstrate distinct dynamic behaviors: BL mitochondria are static and have a high fusion rate, whereas CEN mitochondria are highly motile and fuse less often (Figure 3K). Furthermore, the two populations do not exchange content, suggesting that they may have different biological functions.

CEN Mitochondrial Dynamics Are Selectively Regulated during Exocytosis

We next examined mitochondrial response to increased energy demand during exocytosis. Mitochondria in cytosolic-GFP mice were labeled with MitoTracker, and 4D-IVM was performed during ISO

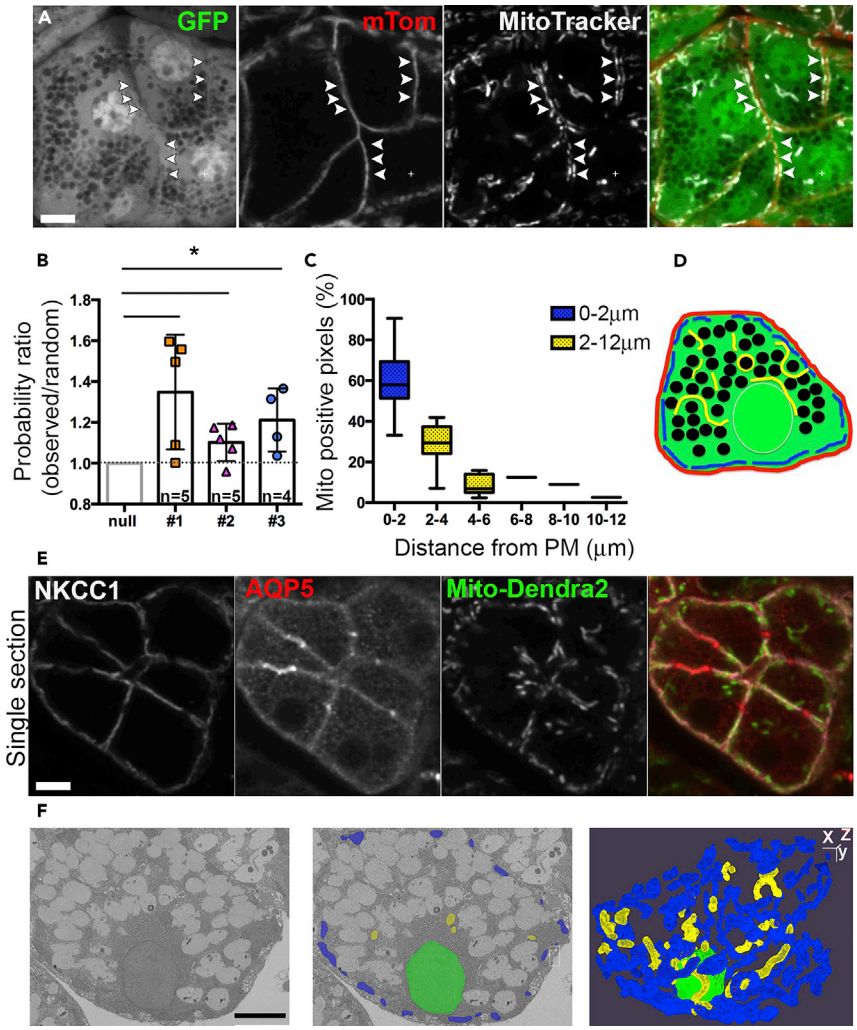

Figure 2. Mitochondrial Distribution in SGs

(A) Optical section of an acinus from cytosolic-GFP/mTom mouse (green and red, respectively) labeled with MitoTracker (white). Arrowheads show mitochondria along the PM (Videos S2 and S3).

(B) Probability ratio was calculated as described in Transparent Methods.

(C) Mitochondria-positive pixels are plotted as a function of distance from the PM. Mitochondria within 2 µm from the PM are labeled in blue and the rest in yellow.

(D) Diagram of an acinar cell illustrating color-coded mitochondrial distribution.

(E) Immunofluorescence labeling of NKCC1 (white, BL) and AQP5 (red, apical) in Mito-Dendra2 mouse (green) (Video S4).

(F) FIB-SEM of mitochondrial distribution and connectivity. Left, section of an acinar cell; center, segmentation of mitochondria (blue and yellow) and nuclei (green) (Video S5); right, volume rendering of the stack (Video S6).

Results are shown as mean ± SEM for N number of cells in three mice, *$p < 0.05$ unpaired t test. Scale bar, 5 µm.

stimulation. Under these conditions, motility of CEN mitochondria increased 2-fold, whereas BL mitochondria remain immobile (Figures 4A and 4B and Video S11). However, BL and CEN mitochondrial distribution was unaffected (Figure S3C). Furthermore, increased motility was not observed in other organelles such as lipid droplets (labeled with BODIPY; Figure S3B), suggesting that the effect is specific to mitochondria. To test whether the rise in CEN mitochondrial motility was also associated with increased mitochondrial fusion, we photo-converted a subset of BL or CEN mitochondria in Mito-Dendra2 mice, injected ISO, and imaged for up to 30 min using 4D-IVM (Figures 4C–4H and Video S12). Fusion events in CEN mitochondria occurred after ISO stimulation (Figures 4F and 4G, arrowheads and line scans, respectively; Figure S3D) and were observed in independent experiments (Figure 4I). Figure 4D shows the time course of converted CEN mitochondria as fold change in volume over time, which also

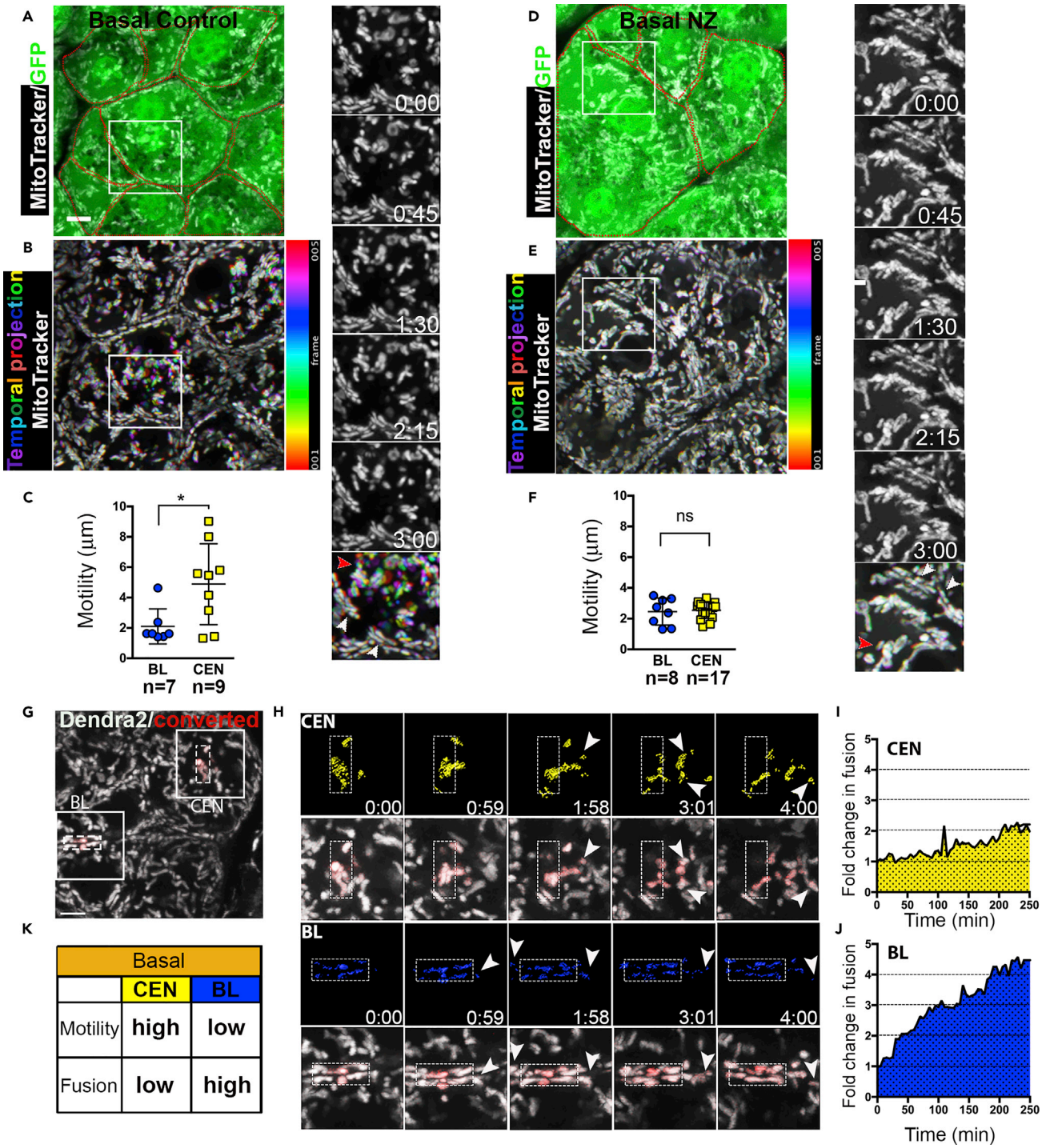

Figure 3. Mitochondrial Dynamics under Basal Conditions

(A–F) 4D-IVM of mitochondria labeled with MitoTracker (white) in cytosolic-GFP (green) mice, either untreated (A–C and Video S7) or treated with 33 µm nocodazole (NZ; D–F and Video S8). Time in min: sec. Dashed red line marks outlines of cells. Insets at different time points over 3 min. (B and E) Temporal color coding and projection of whole frames and insets (last inset at the bottom; temporal projection of static mitochondria will show white mitochondria, whereas moving mitochondria will show color). Red and white arrowheads point CEN and static BL mitochondria, respectively. (C) Quantification of BL (blue) and CEN (yellow) mitochondrial motility (Figures S2A–S2G). (F) BL (blue) and CEN (yellow) motility in the presence of NZ. Representative experiments are shown as mean ± SEM for N mitochondrial clusters; significance was calculated using unpaired t test *$p < 0.05$; ns, $p > 0.05$. Scale bar, 5 µm.

Figure 3. *Continued*

(G–J) Photo conversion of CEN and BL mitochondria in Mito-Dendra2 mice. (G) Converted areas are marked by a white rectangle, and insets are shown for each population. (H) Converted fluorescence is shown as volumes (CEN in yellow and BL in blue) or merged image of converted (red) and MitoDendra2 (white). Arrowheads show mitochondria containing converted Dendra2 outside of the original converted region (white line). Time is shown in hours: min (see Video S10). (I and J) Fold change in fusion over time in CEN (I; yellow) and BL (J; blue) mitochondria.

(K) Table summarizing mitochondrial dynamics under basal conditions. Scale bar, 5 μm.

correlated temporally with the increase in number of exocytic events (Figure 4D; separate experiment plotted on right y axis). Conversely, changes in BL mitochondrial motility and fusion were undetectable (Figures 4A–4C and 4G). A table summarizing mitochondrial dynamic responses during exocytosis is shown in Figure 4I.

Finally, because CEN mitochondrial motility was MT dependent (Figure 3D), we investigated NZ effects on CEN mitochondrial dynamics during exocytosis. We found that NZ blocked the increase in motility (Figure 4K) and fusion (Figures 4L and 4M and Video S13) in CEN mitochondria following stimulation with ISO. Additionally, NZ treatment inhibited exocytosis (Figures 4M and S3E) but had no obvious effect on granule number and distribution, suggesting that selective rearrangement of CEN mitochondria may be important for sustaining exocytosis.

DISCUSSION

Mitochondrial morphology, connectivity, and distribution vary greatly within and between cells in different tissues (Collins et al., 2002; Glancy et al., 2015; Woods, 2017). Here, we describe a conserved mitochondrial distribution in exocrine glands, which includes a prominent mitochondrial belt within 2 μm of the basolateral membrane and a subset of mitochondria dispersed in the cytosol (Figures 2 and S1). Earlier studies in isolated exocrine cells described three mitochondrial populations with distinct functions including mitochondrial population surrounding the granules (Park et al., 2001; Sampson and Montalvo, 1983); however, in this study we found only two populations (Figures 2 and S1). This discrepancy is likely due to artificial changes in mitochondrial positioning induced by the isolation process. Nevertheless, it is still not clear what determines the unique positioning of mitochondria in exocrine tissues. We found that disrupting neither the actin cytoskeleton nor the MT network affected mitochondrial distribution, suggesting that other tethering mechanisms are involved. An attractive possibility is that mitochondrial positioning is facilitated through tethering to the ER (Kornmann et al., 2009; Swayne et al., 2011); however, we were unsuccessful in resolving whether this is the case (Figures S2K and S2L). Additionally, studies on the transcription factor Mist1 proposed that it had a role in organelle positioning in secretory organs (Lo et al., 2017; Luo et al., 2005), although the specific genes involved are not known.

Changes in mitochondrial morphology through motility, fission, and fusion have functional consequences on cells' bioenergetic capacity (Friedman and Nunnari, 2014; Liesa and Shirihai, 2013). Using 4D-IVM, we show that exocytosis triggered a rapid (minutes), selective response in mitochondrial dynamics. Specifically, CEN mitochondrial motility and fusion increased in a MT-dependent manner (Figures 4K–4M). MTs are required for mitochondrial motility (Anesti and Scorrano, 2006); thus, it is likely that in the presence of NZ, fusion was blocked because mitochondria could not move closer for fusion to occur. On the other hand, BL mitochondrial motility and fusion remained unchanged during exocytosis (Figures 4A–4C and 4G). Stationary mitochondria were reported to have lower probability for fusion (Twig et al., 2008, 2010), however, we found that despite their immobility, BL mitochondria exhibited faster fusion rate than the highly motile CEN mitochondria (Figures 3G–3K). In the absence of nutrients, mitochondria undergo fusion, giving rise to a tubular network that is more efficient in ATP production (Gomes et al., 2011; Rambold et al., 2011). Similarly, the increased fusion in CEN mitochondria may represent an adaptation mechanism to the increased energy demand. Indeed, the cellular energy sensor AMPK is activated 5 min after ISO stimulation (Figure 1F), consistent with rapid depletion of cellular ATP during exocytosis. Furthermore, inhibition of the ATP synthase inhibits exocytosis (Figures 1D and 1E), reinforcing the notion that adaptation in ATP production is necessary to sustain exocytosis. NZ treatment not only inhibited CEN mitochondrial fusion but also significantly inhibited exocytosis (Figure 4N), suggesting that fusion of CEN mitochondria is indeed involved in sustaining exocytosis. Control and NZ-treated cells had a comparable number of secretory granules at the apical pole, indicating that the reduced exocytosis was not due to trafficking impairment. However, we do not know whether the

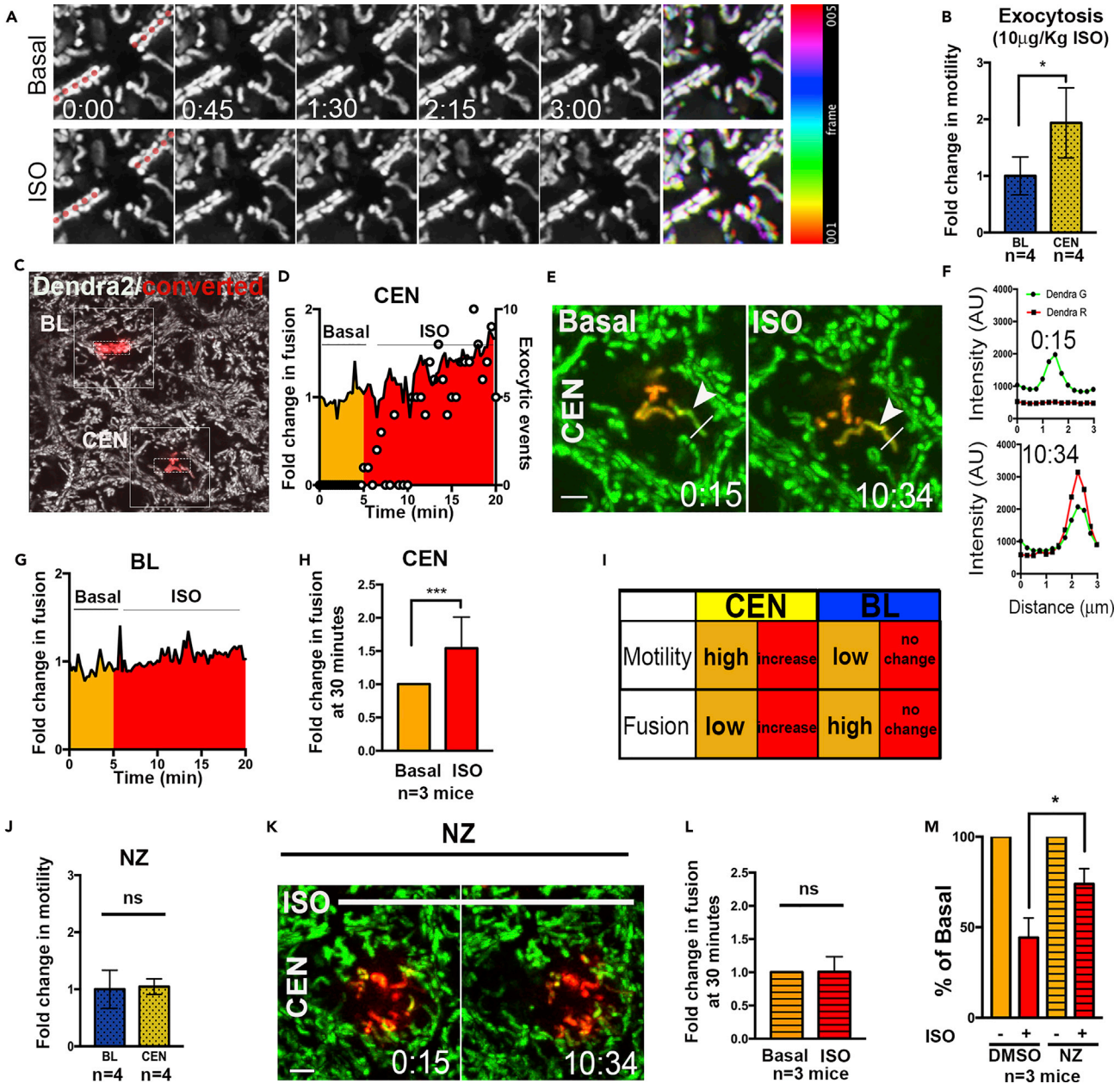

Figure 4. Increased Motility and Volume in CEN Mitochondria during Exocytosis

(A) 4D-IVM of mitochondria labeled with MitoTracker (white), under basal and ISO stimulation (Video S11). Maximal projection images shown; red dotted lines highlight basolateral membrane, along which BL mitochondria align. Right panels show temporal color coding as described in Transparent Methods.

(B and C) (B) Fold change in BL (blue) and CEN (yellow) motility following stimulation of exocytosis (C). Photo conversion of CEN or BL mitochondria (white rectangle) in Mito-Dendra2 mice.

(D) Fold change in CEN mitochondrial fusion 5 min before (orange) and 15 min after (red) ISO stimulation. Right y axis, number of exocytic events, quantified using cytosolic-GFP mice (white circles).

(E) Converted CEN mitochondria from (C) before (0:15) and after (10:34) ISO stimulation. Arrowheads show CEN mitochondrial fusion (Video S12).

(F) Fluorescence intensity (red: converted Dendra2; green: non-converted Dendra2) in line scan from (E) before (0:15) and after (10:34) ISO stimulation.

(G) Fold change in BL mitochondrial fusion 5 min before (orange) and 15 min after (red) stimulation with ISO.

(H) Fold change in CEN mitochondrial fusion calculated by comparing CEN mitochondria converted Dendra2 volume before and 30 min after ISO (see Transparent Methods).

(I) Table summarizing mitochondrial motility and fusion under basal and stimulated conditions.

(J–M) Effect of NZ treatment on CEN mitochondrial dynamics and exocytosis. (J) Fold change in BL (blue) and CEN (yellow) motility following ISO in NZ-treated mice (33 μM). (K) Inset of converted CEN mitochondria from NZ-treated mice (Video S13) are shown before (0:15) and after (10:34) ISO showing

Figure 4. *Continued*

inhibition of CEN mitochondrial fusion. (L) Fold change in CEN mitochondrial fusion calculated by comparing CEN mitochondria converted Dendra2 volume, in NZ-treated mice, before and 30 min after ISO (see Transparent Methods). (M) SGs in cytosolic-GFP mice were treated with DMSO or 33 μM NZ followed by injection of saline or ISO. Exocytosis was evaluated by plotting the normalized number of granules, expressed as percent of the number of granules under basal conditions, 30 min after stimulation. Representative experiments are shown as mean ± SEM for N number of mitochondrial clusters (B and J) or mice (H, L, and M).

Significance was calculated using unpaired t test *$p < 0.05$; ***$p < 0.0005$; ns, $p > 0.05$. Scale bar, 5 μm.

reduced exocytosis is a direct outcome of blocking CEN mitochondrial fusion. Finally, we show that β-adrenergic signaling elicits exocytosis and at the same time promotes CEN mitochondrial dynamic responses and perhaps, ATP production. β-Adrenergic regulation of mitochondrial dynamics and bioenergetics also occurs in cardiomyocytes (Coronado et al., 2018; Xu et al., 2016) and brown adipocytes (Wikstrom et al., 2014), suggesting that this pathway may serve as a conserved regulatory mechanism for cells and tissues to adapt to changes in energy demand.

Mitochondrial transport to sites where ATP is required was shown in multiple cells (Desai et al., 2013; Misgeld and Schwarz, 2017; Quintana and Hoth, 2012) and is facilitated by motors and linkers that move mitochondria along MT tracks (Saxton and Hollenbeck, 2012). In the SGs, CEN mitochondrial motility under basal and stimulated conditions is MT dependent (Figures 3D–3F and 4J); however, we did not observe long-distance transport to the apical pole, where exocytosis occurs. In fact, the apical pole is largely deprived of mitochondria under basal and stimulated conditions (Figures 2E and 4A, and Video S11), suggesting that mitochondria may be optimally positioned to supply the energy required for exocrine functions.

Our data suggest differential roles for the two mitochondrial populations based on their positioning and dynamic responses. We found that CEN and BL have distinct positioning and dynamic properties and rarely fuse with each other. It is likely that the reduced fusion of CEN mitochondria under basal conditions allows their segregation from BL mitochondria, as was recently shown by Benador et al. in brown adipose tissue (Benador et al., 2018). Indeed, this differential regulation of mitochondrial dynamics may give rise to distinct mitochondrial populations and support the idea of distinct functions. Taken together, studying the spatial and temporal changes in mitochondrial dynamics in an intact, actively secreting exocrine gland revealed underappreciated heterogeneity in mitochondrial positioning and dynamics. These findings underscore the importance of studying mitochondrial dynamics *in vivo*, in real time, and in the context of intact tissues and their activities. 4D-IVM provides a unique opportunity to perform these studies under both physiological and pathological conditions.

Limitations of the Study

Inhibition of MTs using NZ may inhibit exocytosis independently of CEN mitochondrial fusion.

METHODS

All methods can be found in the accompanying Transparent Methods supplemental file.

DATA AND SOFTWARE AVAILABILITY

The FIB-SEM imaging data that support findings of this study are available in the National Cancer Institute Center for Stratigic Scientific Initiatives Data Coordinating Center (http://cssi-dcc.nci.nih.gov/cssiportal/view/5c0aeddc34b81e73d5f13a29).

SUPPLEMENTAL INFORMATION

Supplemental Information includes Transparent Methods, 3 figures, and 13 videos and can be found with this article online at https://doi.org/10.1016/j.isci.2018.12.036.

ACKNOWLEDGMENTS

We would like to thank Yun Chen and Alexandra Badiceanu (JHU) for help with mitochondrial distribution analysis. We would like to thank Drs. Youle, Donaldson, Arias and Ebrahim for critical reading of the manuscript. This work was part of N.P.S.'s K99/R00 award and supported by the Intramural Research Program at the NIH, National Institute of Dental and Craniofacial Research, and National Cancer Institute.

This project has been funded in whole or in part with Federal funds from the National Cancer Institute, National Institutes of Health, under Contract No. HHSN261200800001E. The content of this publication does not necessarily reflect the views or policies of the Department of Health and Human Services, nor does mention of trade names, commercial products, or organizations imply endorsement by the US Government.

AUTHOR CONTRIBUTIONS

N.P.S. conceived the project under the supervision of R.W. N.P.S., O.J.H., and L.M. performed the experiments and analyzed the data. FIB-SEM was done by K.N. and analyzed by N.P.S. and L.M. N.P.S. wrote the manuscript. R.W., O.J.H., and L.M. read it and provided feedback.

DECLARATION OF INTERESTS

The authors declare no competing interest.

Received: June 11, 2018
Revised: October 14, 2018
Accepted: December 28, 2018
Published: January 25, 2019

REFERENCES

Anesti, V., and Scorrano, L. (2006). The relationship between mitochondrial shape and function and the cytoskeleton. Biochim. Biophys. Acta *1757*, 692–699.

Benador, I.Y., Veliova, M., Mahdaviani, K., Petcherski, A., Wikstrom, J.D., Assali, E.A., Acin-Perez, R., Shum, M., Oliveira, M.F., Cinti, S., et al. (2018). Mitochondria bound to lipid droplets have unique bioenergetics, composition, and dynamics that support lipid droplet expansion. Cell Metab. *27*, 869–885.e6.

Collins, T.J., Berridge, M.J., Lipp, P., and Bootman, M.D. (2002). Mitochondria are morphologically and functionally heterogeneous within cells. EMBO J. *21*, 1616–1627.

Coronado, M., Fajardo, G., Nguyen, K., Zhao, M., Kooiker, K., Jung, G., Hu, D.Q., Reddy, S., Sandoval, E., Stotland, A., et al. (2018). Physiological mitochondrial fragmentation is a normal cardiac adaptation to increased energy demand. Circ. Res. *122*, 282–295.

Desai, S.P., Bhatia, S.N., Toner, M., and Irimia, D. (2013). Mitochondrial localization and the persistent migration of epithelial cancer cells. Biophys. J. *104*, 2077–2088.

Faits, M.C., Zhang, C., Soto, F., and Kerschensteiner, D. (2016). Dendritic mitochondria reach stable positions during circuit development. Elife *5*, e11583.

Friedman, J.R., and Nunnari, J. (2014). Mitochondrial form and function. Nature *505*, 335–343.

Glancy, B., Hartnell, L.M., Malide, D., Yu, Z.X., Combs, C.A., Connelly, P.S., Subramaniam, S., and Balaban, R.S. (2015). Mitochondrial reticulum for cellular energy distribution in muscle. Nature *523*, 617–620.

Gomes, L.C., Di Benedetto, G., and Scorrano, L. (2011). During autophagy mitochondria elongate, are spared from degradation and sustain cell viability. Nat. Cell Biol. *13*, 589–598.

Hoppins, S. (2014). The regulation of mitochondrial dynamics. Curr. Opin. Cell Biol. *29*, 46–52.

Kornmann, B., Currie, E., Collins, S.R., Schuldiner, M., Nunnari, J., Weissman, J.S., and Walter, P. (2009). An ER-mitochondria tethering complex revealed by a synthetic biology screen. Science *325*, 477–481.

Liesa, M., and Shirihai, O.S. (2013). Mitochondrial dynamics in the regulation of nutrient utilization and energy expenditure. Cell Metab. *17*, 491–506.

Lo, H.G., Jin, R.U., Sibbel, G., Liu, D., Karki, A., Joens, M.S., Madison, B.B., Zhang, B., Blanc, V., Fitzpatrick, J.A., et al. (2017). A single transcription factor is sufficient to induce and maintain secretory cell architecture. Genes Dev. *31*, 154–171.

Luo, X., Shin, D.M., Wang, X., Konieczny, S.F., and Muallem, S. (2005). Aberrant localization of intracellular organelles, Ca2+ signaling, and exocytosis in Mist1 null mice. J. Biol. Chem. *280*, 12668–12675.

Masedunskas, A., Porat-Shliom, N., and Weigert, R. (2012). Linking differences in membrane tension with the requirement for a contractile actomyosin scaffold during exocytosis in salivary glands. Commun. Integr. Biol. *5*, 84–87.

Masedunskas, A., Sramkova, M., Parente, L., Sales, K.U., Amornphimoltham, P., Bugge, T.H., and Weigert, R. (2011). Role for the actomyosin complex in regulated exocytosis revealed by intravital microscopy. Proc. Natl. Acad. Sci. U S A *108*, 13552–13557.

Misgeld, T., and Schwarz, T.L. (2017). Mitostasis in neurons: maintaining mitochondria in an extended cellular architecture. Neuron *96*, 651–666.

Murley, A., and Nunnari, J. (2016). The emerging network of mitochondria-organelle contacts. Mol. Cell *61*, 648–653.

Narayan, K., Danielson, C.M., Lagarec, K., Lowekamp, B.C., Coffman, P., Laquerre, A., Phaneuf, M.W., Hope, T.J., and Subramaniam, S. (2014). Multi-resolution correlative focused ion beam scanning electron microscopy: applications to cell biology. J. Struct. Biol. *185*, 278–284.

Park, M.K., Ashby, M.C., Erdemli, G., Petersen, O.H., and Tepikin, A.V. (2001). Perinuclear, perigranular and sub-plasmalemmal mitochondria have distinct functions in the regulation of cellular calcium transport. EMBO J. *20*, 1863–1874.

Porat-Shliom, N., Chen, Y., Tora, M., Shitara, A., Masedunskas, A., and Weigert, R. (2014). In vivo tissue-wide synchronization of mitochondrial metabolic oscillations. Cell Rep. *9*, 514–521.

Proctor, G.B., and Carpenter, G.H. (2014). Salivary secretion: mechanism and neural regulation. Monogr. Oral Sci. *24*, 14–29.

Quintana, A., and Hoth, M. (2012). Mitochondrial dynamics and their impact on T cell function. Cell Calcium *52*, 57–63.

Rambold, A.S., Kostelecky, B., Elia, N., and Lippincott-Schwartz, J. (2011). Tubular network formation protects mitochondria from autophagosomal degradation during nutrient starvation. Proc. Natl. Acad. Sci. U S A *108*, 10190–10195.

Sampson, H.W., and Montalvo, A.M. (1983). Association of mitochondria with the plasma membrane of the acinar cells of actively secreting and nonsecreting rat lacrimal and parotid glands. Acta Anat. (Basel) *116*, 353–357.

Saxton, W.M., and Hollenbeck, P.J. (2012). The axonal transport of mitochondria. J. Cell Sci. *125*, 2095–2104.

Schuler, M.H., Lewandowska, A., Caprio, G.D., Skillern, W., Upadhyayula, S., Kirchhausen, T., Shaw, J.M., and Cunniff, B. (2017). Miro1-mediated

mitochondrial positioning shapes intracellular energy gradients required for cell migration. Mol. Biol. Cell *28*, 2159–2169.

Smit-Rigter, L., Rajendran, R., Silva, C.A., Spierenburg, L., Groeneweg, F., Ruimschotel, E.M., van Versendaal, D., van der Togt, C., Eysel, U.T., Heimel, J.A., et al. (2016). Mitochondrial dynamics in visual cortex are limited in vivo and not affected by axonal structural plasticity. Curr. Biol. *26*, 2609–2616.

Swayne, T.C., Zhou, C., Boldogh, I.R., Charalel, J.K., McFaline-Figueroa, J.R., Thoms, S., Yang, C., Leung, G., McInnes, J., Erdmann, R., et al. (2011). Role for cER and Mmr1p in anchorage of mitochondria at sites of polarized surface growth in budding yeast. Curr. Biol. *21*, 1994–1999.

Twig, G., Elorza, A., Molina, A.J., Mohamed, H., Wikstrom, J.D., Walzer, G., Stiles, L., Haigh, S.E., Katz, S., Las, G., et al. (2008). Fission and selective fusion govern mitochondrial segregation and elimination by autophagy. EMBO J. *27*, 433–446.

Twig, G., Liu, X., Liesa, M., Wikstrom, J.D., Molina, A.J., Las, G., Yaniv, G., Hajnoczky, G., and Shirihai, O.S. (2010). Biophysical properties of mitochondrial fusion events in pancreatic beta-cells and cardiac cells unravel potential control mechanisms of its selectivity. Am. J. Physiol. Cell Physiol. *299*, C477–C487.

Westermann, B. (2012). Bioenergetic role of mitochondrial fusion and fission. Biochim. Biophys. Acta *1817*, 1833–1838.

Wikstrom, J.D., Mahdaviani, K., Liesa, M., Sereda, S.B., Si, Y., Las, G., Twig, G., Petrovic, N., Zingaretti, C., Graham, A., et al. (2014). Hormone-induced mitochondrial fission is utilized by brown adipocytes as an amplification pathway for energy expenditure. EMBO J. *33*, 418–436.

Woods, D.C. (2017). Mitochondrial heterogeneity: evaluating mitochondrial subpopulation dynamics in stem cells. Stem Cells Int. *2017*, 7068567.

Xu, S., Wang, P., Zhang, H., Gong, G., Gutierrez Cortes, N., Zhu, W., Yoon, Y., Tian, R., and Wang, W. (2016). CaMKII induces permeability transition through Drp1 phosphorylation during chronic beta-AR stimulation. Nat. Commun. *7*, 13189.

Youle, R.J., and van der Bliek, A.M. (2012). Mitochondrial fission, fusion, and stress. Science *337*, 1062–1065.

ISCI, Volume *11*

Supplemental Information

Mitochondrial Populations Exhibit Differential Dynamic Responses to Increased Energy Demand during Exocytosis *In Vivo*

Natalie Porat-Shliom, Olivia J. Harding, Lenka Malec, Kedar Narayan, and Roberto Weigert

Supplemental Data

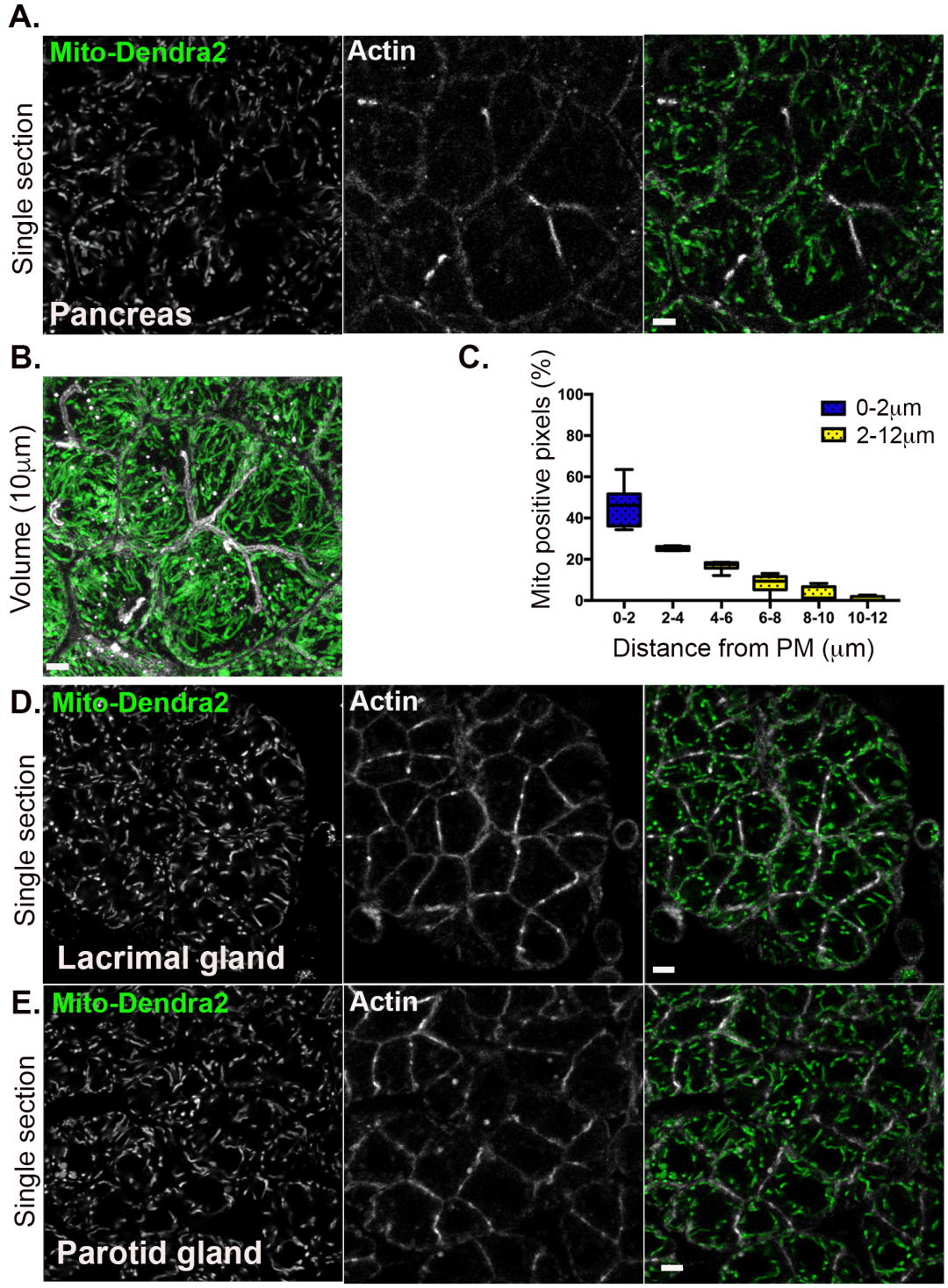

Figure S1: Mitochondrial distribution is conserved in exocrine glands (related to Fig 2). Exocrine organs from Mito-Dendra2 mice (pancreas, lacrimal and parotid glands) were labeled with phalloidin. **A.** Single sections showing mitochondria and actin in the pancreas, lacrimal gland (**D.**)

and parotid gland (**E.**). **B.** Volume projection of the section in A. **C.** Mitochondrial distribution analysis in the pancreas. Scale bar 5μm.

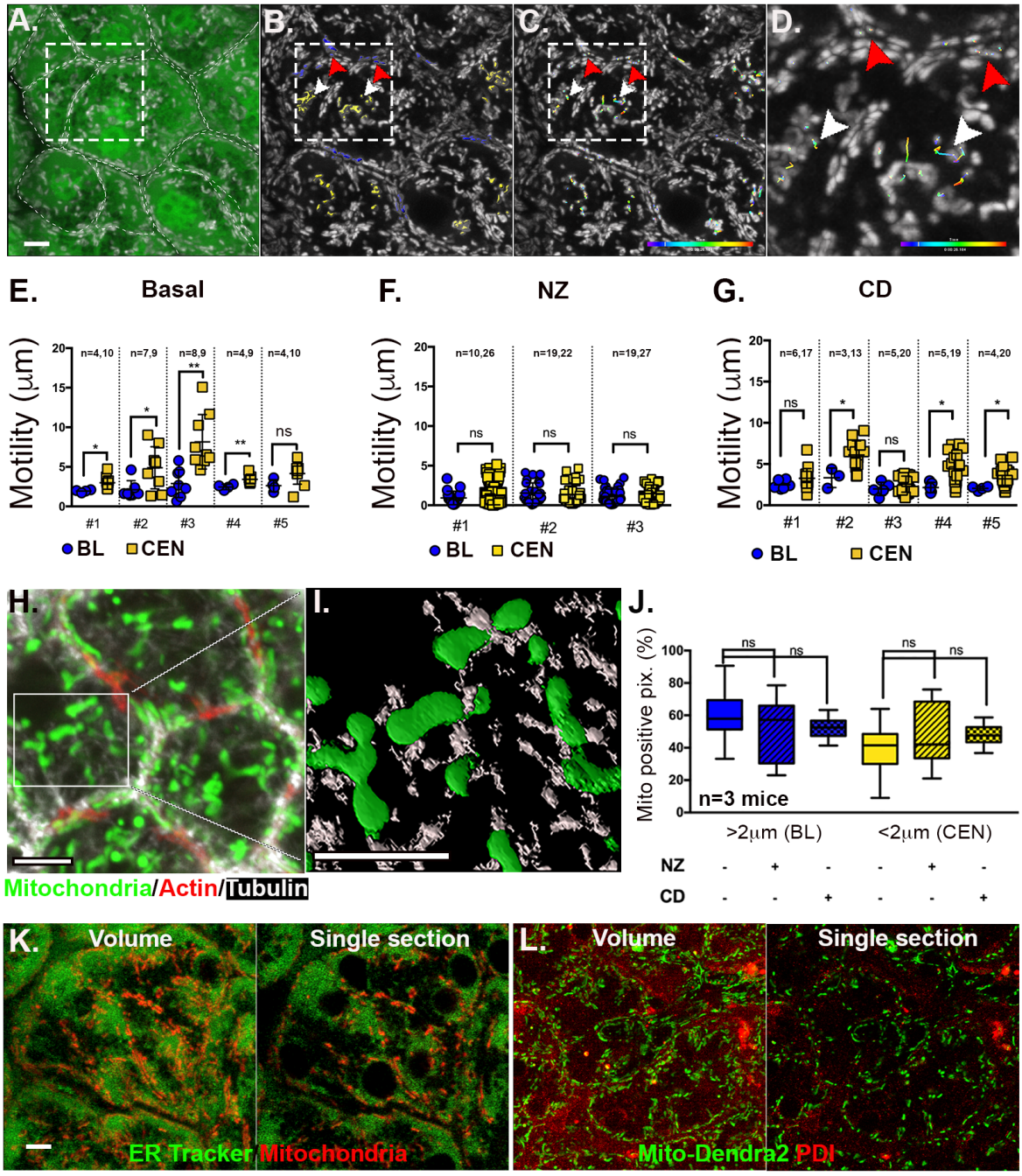

Figure S2: Quantification of mitochondrial motility and distribution *in vivo* (related to Fig 3). A. Overlay of cytosolic-GFP, MitoTracker (white) and dashed white line to mark outlines of cells in a single max-projected frame from 4D-IVM time-lapse series. **B.** Overlay of MitoTracker and volumes generated in Imaris for BL (blue; red arrowheads) or CEN (yellow; white arrowheads). **C.** MitoTracker, center of volumes (yellow dot) and temporally color-coded tracks 'traveled' by each volume in the mitochondria cluster over 150 seconds are shown. **D.** High magnification of inset

in C. **E-G.** Mitochondria motility (μm) in BL (blue) and CEN (yellow) under basal, nocodazole (NZ; F) and cytochalasin D (CD; G) treatment in different mice. **H.** Immunofluorescence of tubulin (white) and actin (red) in Mito-Dendra2 (green) mouse. **I.** Volume rendering of mitochondria (green) and microtubules (white) (Movie S9). **J.** Analysis of mitochondrial distribution in control (non-treated), NZ and CD treated glands. **K.** Localization of mitochondria *in vivo* (Mito-Tracker-Red) and ER (ER-Tracker Green) **L.** localization of mitochondria (Mito-Dendra2, green) and ER (antibody against PDI, red) in fixed SGs. Representative images of 5μm max-projected volumes or single optical section are shown. Results are shown as Mean ± SEM for N number of mitochondria clusters (E-G) in 3-5 mice, as indicated. Significance was calculated using unpaired t-test *$p<0.05$; **$p<0.005$; ns, $p>0.05$. Scale bar 5μm.

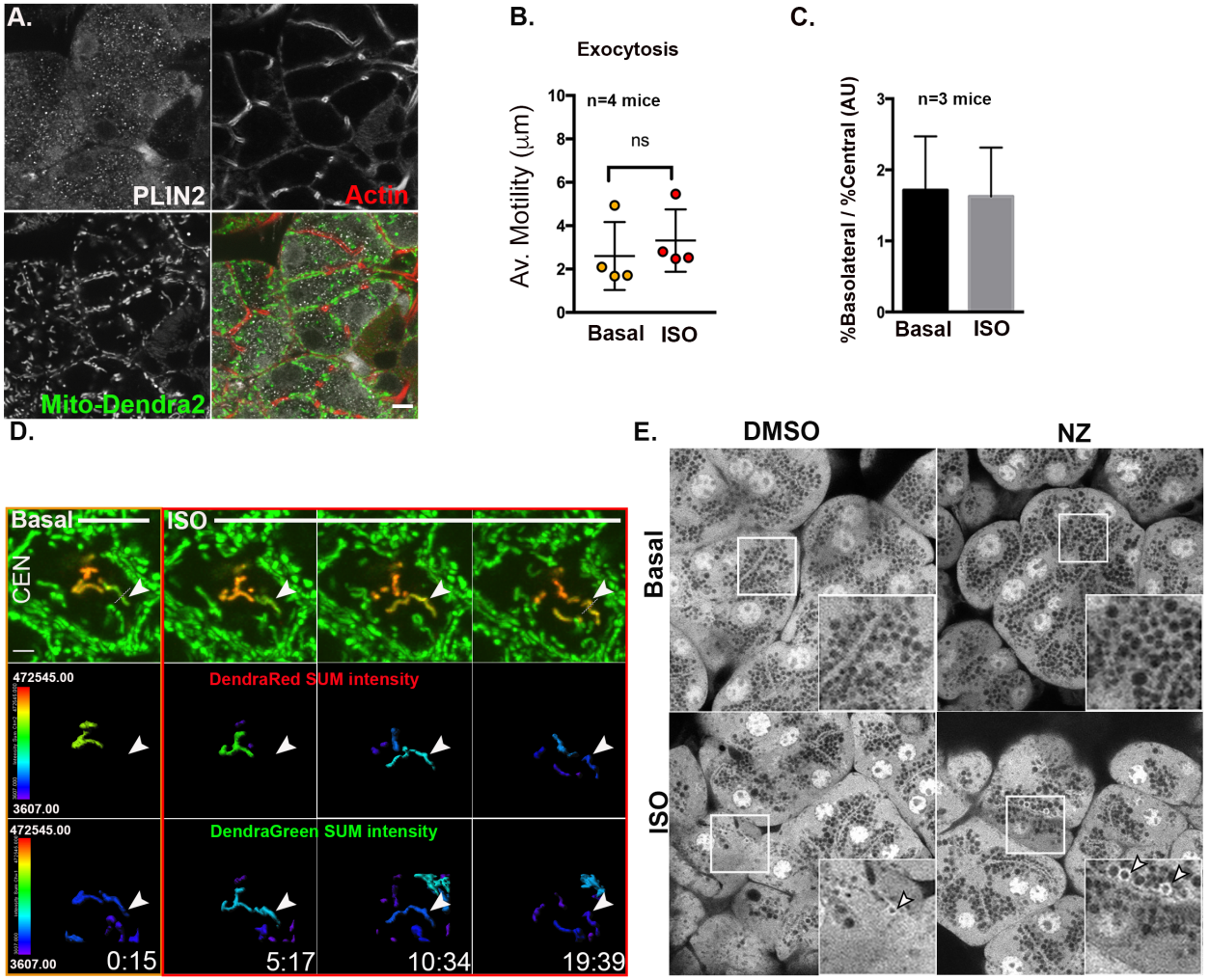

Figure S3: Lipid droplet and mitochondrial dynamics during exocytosis (related to Fig 4). A. Fixed SG sections from Mito-Dendra2 (green) mouse were labeled with anti-Perilipin 2 (PLIN2, white) and phalloidin (red) to determine lipid droplets distribution. **B.** Average lipid droplet motility was measured before (basal) and after ISO stimulation by labeling lipid droplets with BODIPY and tracking over time. **C.** Mitochondrial distribution was calculated as the ratio between percent BL mitochondria over percent CEN mitochondria, under basal and stimulated conditions. **D.** Representative frames from Movie S12 before and after ISO stimulation showing CEN mitochondria fusion (arrowheads, upper and middle rows). Sum intensity of converted Dendra2 (DendraRed; middle row) and Sum intensity of non-converted Dendra2 (DendraGreen; lower row) show decrease in sum intensity in DendraRed but not DendraGreen indicative of mitochondria fusion. **E.** DMSO or 33μM NZ treated SGs in cytosolic-GFP mice injected with saline (control) or ISO. Arrowheads point to exocytic events. Representative images, from those used

for quantification in Fig 4M, are shown. Arrowheads point to secretory granules undergoing exocytosis. Results are shown as Mean ± SEM for N number of mice, as indicated. Significance was calculated using unpaired t-test *p<0.05; **p<0.005; ns, p>0.05. Scale bar 5μm.

Transparent Methods

KEY RESOURCES TABLE

REAGENT or RESOURCE	SOURCE	IDENTIFIER
Fluorescent probes		
Rhodamine phalloidin	ThermoFisher Scientific (Waltham, MA).	catalog no. R415
MitoTracker Deep Red FM	ThermoFisher	catalog no. M22426
ER-Tracker Green	ThermoFisher	catalog no. E34251
BODIPY 493/503	ThermoFisher	catalog no. D3922
BODIPY 665/676	ThermoFisher	catalog no. B3932
Antibodies		
goat anti-rabbit Alexa Fluor 647	ThermoFisher	catalog no. A21245
goat anti-mouse Alexa Fluor 647	ThermoFisher	catalog no. A21235
goat anti-mouse Alexa Fluor 594	ThermoFisher	catalog no. A11005
goat polyclonal antibody against NKCC1	Santa Cruz Biotechnology (Dallas, TX)	catalog no. 21545
rabbit polyclonal antibody against aquaporin 5	Santa Cruz Biotechnology	catalog no. 28628
mouse monoclonal antibody against α-tubulin	Santa Cruz Biotechnology	catalog no. 8035
rabbit polyclonal antibodies against β-tubulin	Cell Signaling Technology (Danvers, MA)	catalog no. 2128
rabbit polyclonal antibody against AMPK	Cell Signaling Technology	catalog no. 2532
Rabbit monoclonal antibody against phosph-Thr172AMPK	Cell Signaling Technology	catalog no. 2535
rabbit polyclonal antibody against PDI	Cell Signaling Technology	catalog no. 2446
anti-mouse IgG HRP-linked secondary antibody	Cell Signaling Technology	catalog no. 7076
anti-rabbit IgG HRP-linked secondary antibody	Cell Signaling Technology	catalog no. 7074
Chemicals		
Nocodazole	Sigma-Aldrich (St. Louis, MO)	catalog no. M1404
Isoproterenol	Sigma-Aldrich	catalog no. 1351005

cytochalasin D	Sigma-Aldrich	catalog no. C8273
oligomycin	Sigma-Aldrich	catalog no. 75351
rotenone	Sigma-Aldrich	catalog no. R8875
Deposited Data		
FIB-SEM Imaging of Acinar Cells of the Mouse Salivary Gland	National Cancer Institute Center for Strategic Scientific Initiatives Data Coordinating Center	https://cssi-dcc.nci.nih.gov/cssiportal/view/5c0aeddc34b81e73d5f13a20
Experimental Models: Organisms/Strains		
Wild-type FVB	The Jackson Laboratory	Stock no. 001800
PhaM excised	The Jackson Laboratory	Stock No: 018397
cytosolic-GFP	The Jackson Laboratory	Stock No: 008200
tandem-Tomato membrane (mTom)	The Jackson Laboratory	Stock No: 007576
Software and Algorithms		
Imaris	Bitplane Inc.	NA
Fiji		NA
Prism	GraphPad	NA

Contact for Reagent and Resource Sharing

Please contact Natalie Porat-Shliom (Natalie.porat-shliom@nih.gov) or Roberto Weigert (weigertr@mail.nih.gov) for reagent and resource requests.

Mice and 4D-IVM

The study was approved and conducted according to the animal protocols approved by the Institutional Animal Care and Use Committee, protocols 15-779 (National Institute of Dental and Craniofacial Research), LCMB-031 and LCMB-037 (National Cancer Institute), in compliance with the Guide for the Care and Use of Laboratory Animals (National Institutes of Health publication 86-23, revised 1985). PhaM excised mice were outcrossed with wild-type FVB mice to switch their background to FVB. Cytosolic-GFP and mTom mice were crossed to breed mice that were cytosolic-GFP/mTom. All mice used in this study were females and weighed 20-30 g. Mice were anesthetized by an intraperitoneal (IP) injection of a mixture of 100 mg/Kg ketamine and 20 mg/Kg xylazine. The SGs were externalized, and the body temperature of the mice was maintained at 37°C with heated pads. For labeling of mitochondria and/or lipid droplets, the

exposed glands were bathed in 0.5 μM MitoTracker Deep Red FM (Thermo Fischer Scientific) for 20 minutes and/or in 10 μM BODIPY 493/503 (Thermo Fischer Scientific) for two hours. When these two probes were used together, they were bathed sequentially starting with the MitoTracker. For 4D-IVM, the SG of the anesthetized mice were immobilized on the stage using a custom holder, as previously described (Masedunskas et al., 2013). The stage and objective were maintained at 37°C using an objective heater and a heat pad. The blood flow was assessed visually using the eyepiece. A carbomer-940 based gel (Snowdrift Farm, Tucson, AZ) was applied to the exposed tissue to prevent dehydration. All 4D-IVM were performed using a point-scanning IX81 inverted confocal microscope equipped with a scanning head and a 40X silicon oil immersion lens (Fluoview 1000; Olympus America Inc.). For photo-conversion experiments, rectangular areas containing population of interest (CEN or BL) were selected, and converted with a 10 us/pixel dwelling time, 46% of 405 laser power for 100 milliseconds. Area sizes were not identical in all experiments. Initial experiments were performed to establish the ability to consistently track converted mitochondria within the 5μm stacks imaged, no out-of-plane converted mitochondria appeared. The fold change in photo-converted volume was quantified (see below).

Drug treatment

Exposed SGs were submerged in 33μM Nocodazole, 10μM Rotenone, 1μg/ml Oligomycin, 10μM cytochalasin D or DMSO for 20 min, stimulated with subcutaneous injection of 100μl saline (control) or 10μg/Kg ISO, and imaged using 4D-IVM or excised and imaged. Effective concentrations of rotenone and oligomycin were evaluated by their effect on TMRM and NADH endogenous fluorescence intensities, respectively (Porat-Shliom et al., 2014). At least three fields of view per treatment were acquired and minimum five cells used for quantification in three mice.

Image analysis and quantification

All time-lapse videos were processed in Imaris (Bitplane) and registered using the Correct 3D drift plugin in Fiji (Parslow et al., 2014) to reduce the motion artifacts. Data analysis was performed in Prism (GraphPad) and Excel (Microsoft), p-values were calculated using unpaired t-test.

Quantification of exocytosis

The cytosolic-GFP channel was used to visualize the secretory granules. Granules were counted, normalized to the area of the cell, and expressed as percent of control.

Mitochondrial distribution analysis

Maximal projections of 5μm z-stacks from cytosolic-GFP mouse SGs labeled with MitoTracker. In each image, 3 to 4 cells were selected, cropped and MitoTracker channel was binarized. X-y coordinates of "mitochondria-positive" pixel and cell outlines (for area calculation) were extracted to a text file. A Java program was written to compute the distance between mitochondria-positive pixels and the closest pixel in the cells' outline. To demonstrate significant difference between randomly distributed population and the observed distribution, first the average number of mitochondria-positive pixels per square-micron was calculated for each cell (total number of mitochondria-positive pixels in a cell/ total area of the cell). Then, the same value was calculated using the number of mitochondria-positive pixels within 2 μm of the membrane and the area of the 2 μm-wide belt. The ratio of the latter (actual) distribution to the former (random) distribution could be <1, indicating distribution biased away from the membrane; =1, the null hypothesis, indicating a random distribution; or >1, indicating a distribution biased toward the membrane. The ratio was calculated for each cell, and statistical significance was determined based on an unpaired t-test. For each cell, the numbers of mitochondria-positive pixels at every distance from the membrane were binned in 2 μm increments (i.e. 0 to 2 μm from the membrane, 2 to 4 μm from the membrane…). The results were normalized by determining what percent of the total mitochondria-positive pixels in each cell resided in each of the 2 μm bins.

Quantification of mitochondria and lipid droplet motility

Volume rendering of lipid droplets or mitochondria clusters was created in Imaris (Bitplane) and track length of each volume was recorded for either 150 seconds (for basal experiments) or 150 seconds before and 150 seconds after stimulation (subcutaneous injection of 10μg/Kg ISO) see Sup 2A-D and Sup Fig 3B. In stimulated experiments, only volumes that could be tracked both before and after stimulation, were analyzed. Clusters from at least three cells were analyzed per population, per mouse and change in motility (ratio between track length before and after

stimulation) was calculated. Fold change from at least 3 mice were combined and shown as Mean ± SEM.

Mitochondrial volume measurement

Mitochondria volumes were measured using Imaris (Bitplane), with minor changes of the described approach (Anand et al., 2014). Briefly, a region of interest was selected, volumes generated for the non-converted (green) and converted (red) signals, and the ratio of red/green was used to calculate the fold change in fusion. Due to photo-toxicity, only 5μm stacks were imaged which represent approximately 25-33% of the whole cell volume. Fold change from at least 5 mice were combined and shown as Mean ± SEM. Calculations and unpaired t-test were performed in Excel and Prism, respectively.

Intra-cardiac fixation, tissue processing and immunofluorescence

Intra-cardiac fixation of the SGs was performed by a needle puncture of the left ventricle followed by a puncture of the right atrium. Initial blood wash-out was performed by injecting 25ml PBS into the ventricle, and the tissue was fixed by subsequent injection of 30-35 mL, pre-warmed 4% formaldehyde solution for tissues fixation. Tissues (salivary, parotid, lacrimal glands and pancreas) were excised and submerged in 25-30 mL of 4% formaldehyde overnight at 4°C. The glands were then washed in PBS pH 7.4 and sliced into 50 μm sections using a vibratome (VT1000s; Leica). For immunofluorescence, tissue slices were incubated in a blocking solution of 10% FBS and 0.01% triton in PBS for 60 minutes at room temperature. They were then incubated with primary antibodies in blocking solution for 2 days at 4°C, stained with secondary antibodies in blocking solution overnight in 4°C, and finally stained with phalloidin in PBS for 1 hour at room temperature. Following staining, the tissue was mounted on a glass slide using Fluoromount G with a no.1 coverslip.

Western blot analysis

SGs were excised and "snap-frozen" in liquid nitrogen. The tissue was subsequently lysed in RIPA buffer (150mM NaCl,0.1% Triton X-100, 0.5% sodium deoxycholate, 0.1% sodium dodecyl sulfate, and 50 mM Tris HCl pH 8.0) containing EDTA, PMSF, and Halt Inhibitor Cocktail. Then it was homogenized using an electric tissue homogenizer (Bertin technologies) 3 times at 6500 rpm for 20 seconds. This was followed by centrifugation at 13,000 rpm at 4°C for 20 minutes. Then 20 μg

of protein were separated on 4%-20% sodium dodecyl sulfate-polyacrylamide gel (Bio-Rad, Hercules, CA). Proteins were then transferred on ice for 1 hour at 100 V to nitrocellulose membrane, membranes were blocked in 5% milk-TBS for 1 hour and incubated with primary antibodies at 4°C overnight. Membranes were then washed in TBST and incubated with secondary HRP-conjugated antibodies for 1 hour at room temperature. Membranes were washed in TBST again, and proteins were detected using Immobilon Western Chemiluminescent HRP Substrate (Millipore Corp., Burlington, MA). Films were scanned with an Epson Perfection V600 Photo scanner and quantification of band intensity was measured with ImageJ.

FIB-SEM

FIB-SEM imaging was performed using a Zeiss Crossbeam 540 (Carl Zeiss Inc.) in conjunction with ATLAS3D software (Fibics Inc.) as previously published (Narayan et al., 2014), with a few modifications. Following intra-cardiac fixation, the SGs were excised, thick sectioned and stained by H&E according to standard protocols. They were then fixed in 2.5% glutaraldehyde in 0.1M sodium cacodylate buffer, stained, and resin embedded according to standard EM protocols. Care was taken to embed the tissue “flat side up”, so that the surface most closely resembling the last cut and stained H&E section was exposed. This sample was affixed to an SEM stub with conductive paint and sputter coated with a ~10 nm Au layer. Regions of interest seen in the H&E stained image were then identified by SEM imaging at 3 kV incident energy. These acini were then protected by a ~2 µm thick platinum and carbon patterned protective pad deposited with the FIB operated at 700 pA, and data collection was executed with the FIB and SEM operated simultaneously. The FIB was operated at 30 kV, 1.5 nA and SEM operated at 1.5 kV, 1 nA, and the back-scatter signal was recorded at the in-column EsB detector operated with a 900V grid voltage. Images were acquired at 5 nm pixel sampling and 15 nm milling increments, with total dwell time of 3 µs per pixel. An imaging run covering an entire cell typically lasted ~40 h and generated a stack of ~1400 high resolution images. These images were processed using in-house IMOD based scripts (Kremer et al., 1996) to yield registered, cropped, binned and inverted isotropic .mrc image volumes. Segmentation of individual mitochondria was performed using the TrakEM2 tool in the FIJI software (Cardona et al., 2012).

References for Transparent Methods:

Anand, R., Wai, T., Baker, M.J., Kladt, N., Schauss, A.C., Rugarli, E., and Langer, T. (2014). The i-AAA protease YME1L and OMA1 cleave OPA1 to balance mitochondrial fusion and fission. J Cell Biol *204*, 919-929.

Cardona, A., Saalfeld, S., Schindelin, J., Arganda-Carreras, I., Preibisch, S., Longair, M., Tomancak, P., Hartenstein, V., and Douglas, R.J. (2012). TrakEM2 software for neural circuit reconstruction. PLoS One *7*, e38011.

Kremer, J.R., Mastronarde, D.N., and McIntosh, J.R. (1996). Computer visualization of three-dimensional image data using IMOD. J Struct Biol *116*, 71-76.

Masedunskas, A., Porat-Shliom, N., Tora, M., Milberg, O., and Weigert, R. (2013). Intravital microscopy for imaging subcellular structures in live mice expressing fluorescent proteins. J Vis Exp.

Narayan, K., Danielson, C.M., Lagarec, K., Lowekamp, B.C., Coffman, P., Laquerre, A., Phaneuf, M.W., Hope, T.J., and Subramaniam, S. (2014). Multi-resolution correlative focused ion beam scanning electron microscopy: applications to cell biology. J Struct Biol *185*, 278-284.

Parslow, A., Cardona, A., and Bryson-Richardson, R.J. (2014). Sample drift correction following 4D confocal time-lapse imaging. J Vis Exp.

Porat-Shliom, N., Chen, Y., Tora, M., Shitara, A., Masedunskas, A., and Weigert, R. (2014). In vivo tissue-wide synchronization of mitochondrial metabolic oscillations. Cell Rep *9*, 514-521.